Cooperative phenomenon in a rippled graphene: Chiral spin guide

M. Pudlak,[1] K. N. Pichugin,[2] and R. G. Nazmitdinov[3,4]
[1]*Institute of Experimental Physics, 04001 Kosice, Slovak Republic*
[2]*Kirensky Institute of Physics, 660036 Krasnoyarsk, Russia*
[3]*Departament de Física, Universitat de les Illes Balears, E-07122 Palma de Mallorca, Spain*
[4]*Bogoliubov Laboratory of Theoretical Physics, Joint Institute for Nuclear Research, 141980 Dubna, Russia*
(Received 17 June 2015; revised manuscript received 28 September 2015; published 30 November 2015)

We analyze spin scattering in ballistic transport of electrons through a ripple at a normal incidence of an electron flow. The model of a ripple consists of a curved graphene surface in the form of an arc of a circle connected from the left-hand and right-hand sides to two flat graphene sheets. At certain conditions the curvature-induced spin-orbit coupling creates a transparent window for incoming electrons with one spin polarization simultaneously with a backscattering of those with opposite polarization. This window is equally likely transparent for electrons with spin up and spin down that move in opposite directions. The spin-filtering effect that is small in one ripple becomes prominent with the increase of N consequently connected ripples that create a graphene sheet of the sinusoidal type. We present the analytical expressions for spin-up and spin-down transmission probabilities as a function of N connected ripples.

DOI: 10.1103/PhysRevB.92.205432 PACS number(s): 72.25.−b, 71.70.Ej, 73.23.Ad

I. INTRODUCTION

The extraordinary properties of graphene have attracted enormous experimental and theoretical attention for a decade (see, e.g., Refs. [1,2]). Graphene, being a zero-gap semiconductor, has a band structure described by a linear dispersion relation at low energy, similar to massless Dirac-Weyl fermions. Such a band structure leads to exceptionally high mobility of charged carriers. A question of possible mechanisms that would allow us to throttle the mobility and, consequently, to control conductivity is a topical subject in graphene physics due to its fundamental as well as technological significance.

Among various mechanisms that might affect the mobility, the scattering that could be induced by a ripple (see, for example, discussion in Ref. [3]) appears to be the most natural one since graphene sheets are not perfectly flat. Moreover, periodic ripples can be created and controlled in suspended graphene, in particular, by thermal treatment [4] and by placing graphene in a specially prepared substrate. Indeed, curvature of the surface affects the π orbitals that determine the electronic properties of graphene. It results in enhancement of spin-orbit coupling that could serve as a source of spin scattering. We recall that the intrinsic (intra-atomic) spin-orbit interaction in flat graphene is weak [1,2,5]. It makes spin decoherence in such a material weak as well; that is, scattering due to disorder is supposed to be unimportant. In order to get deep insight into the nature of curvature-induced scattering, it is desirable to elucidate, among many questions, the basic one: What are the distinctive features of curvature-induced spin-orbit coupling? One can further ask how to employ these features to guide electron transport in a graphene-based system at the theoretical and, quite likely, practical levels.

A consistent approach to introduce the curvature-induced spin-orbit coupling (SOC) in the low-energy physics of graphene has been developed by Ando [6] and by others [7–9] in the framework of effective mass and tight-binding approximations. Recent measurements in ultraclean carbon nanotubes (CNTs) [10], i.e., in an extreme form of curved graphene, revealed the energy splitting that can be associated with spin-orbit coupling. The measured shifts are compatible with theoretical predictions [6,9], while some features regarding the contribution of different spin-orbit terms in metallic and nonmetallic CNTs are still debatable (see, for example, discussion in [11–16]). Nowadays, nevertheless, there is a consensus that for armchair CNTs one obtains two SOC terms: one preserves the spin symmetry (a spin projection on the CNT symmetry axis), while the second one breaks this symmetry [6,14,15,17]. Thus, we have a reliable answer to the first question, at least for armchair CNTs. In some previous studies [6,9,14,15] the role played by the second term was underestimated. In this paper we will attempt to answer how full curvature-induced SOC, including the second term, could be used to create a polarized spin current with high efficiency in a rippled graphene system.

The structure of this paper is as follows. In Sec. II we briefly discuss the explicit expressions for the eigenspectrum and eigenfunctions of an armchair nanotube with full curvature-induced spin-orbit coupling. By means of these results we introduce a scattering model for one ripple and extend this model for N continuously connected ripples. In Sec. III we provide a discussion of our results in terms of simple estimates. The main conclusions are summarized in Sec. IV.

II. SCATTERING PROBLEM

In order to model a scattering problem on a ripple we consider a curved surface in the form of an arc of a circle connected from the left-hand and right-hand sides to two flat graphene sheets. The solution for flat graphene is well known [1,2]. The solution for a curved graphene surface can be expressed in terms of the results obtained for armchair CNTs in an effective-mass approximation, when only the interaction between nearest-neighbor atoms is taken into account [17].

A. Low-energy spectrum of the armchair nanotube

Let us recapitulate the major results [17] in the vicinity of the Fermi level $E = 0$ for a point K in the presence of the

curvature-induced spin-orbit interaction in an armchair CNT. The y axis is chosen as the symmetry and the quantization axis. In this case the eigenvalue problem is defined as

$$\hat{H}\Psi = \begin{pmatrix} 0 & \hat{f} \\ \hat{f}^\dagger & 0 \end{pmatrix} \begin{pmatrix} F_A^K \\ F_B^K \end{pmatrix} = E \begin{pmatrix} F_A^K \\ F_B^K \end{pmatrix}, \tag{1}$$

with the following definitions:

$$\begin{aligned} \hat{f} &= \gamma(\hat{k}_x - i\hat{k}_y) + i\frac{\delta\gamma'}{4R}\hat{\sigma}_x(\vec{r}) - \frac{2\delta\gamma p}{R}\hat{\sigma}_y, \\ \hat{k}_x &= -i\frac{\partial}{R\partial\theta}, \quad \hat{k}_y = -i\frac{\partial}{\partial y}, \\ \hat{\sigma}_x(\vec{r}) &= \hat{\sigma}_x\cos\theta - \hat{\sigma}_z\sin\theta. \end{aligned} \tag{2}$$

Here, $\hat{\sigma}_{x,y,z}$ are standard Pauli matrices, and the spinors of two sublattices are

$$F_A^K = \begin{pmatrix} F_{A,\uparrow}^K \\ F_{A,\downarrow}^K \end{pmatrix}, \quad F_B^K = \begin{pmatrix} F_{B,\uparrow}^K \\ F_{B,\downarrow}^K \end{pmatrix}. \tag{3}$$

The following notations are used: $\gamma = -\sqrt{3}V_{pp}^\pi a/2 = \gamma_0 a$, $\gamma' = \sqrt{3}(V_{pp}^\sigma - V_{pp}^\pi)a/2 = \gamma_1 a$, $p = 1 - 3\gamma'/8\gamma$ (see, e.g., Ref. [6]). The quantities V_{pp}^σ and V_{pp}^π are the transfer integrals for σ and π orbitals, respectively, in a flat graphene; $a = \sqrt{3}d \simeq 2.46$ Å is the length of the primitive translation vector, where d is the distance between atoms in the unit cell.

The intrinsic source of the SOC $\delta = \Delta/(3\epsilon_{\pi\sigma})$ is defined as

$$\Delta = i\frac{3\hbar}{4m_e^2c^2}\langle x_l|\frac{\partial V}{\partial x}\hat{p}_y - \frac{\partial V}{\partial y}\hat{p}_x|y_l\rangle, \tag{4}$$

where V is the atomic potential and $\epsilon_{\pi\sigma} = \epsilon_{2p}^\pi - \epsilon_{2p}^\sigma$. The energy ϵ_{2p}^σ is the energy of σ orbitals, localized between carbon atoms. The energy ϵ_{2p}^π is the energy of π orbitals, directed perpendicular to the curved surface.

By means of the unitary transformation

$$\hat{U}(\theta) = \exp\left(i\frac{\theta}{2}\hat{\sigma}_y\right) \otimes I, \tag{5}$$

where I is a 2×2 unity matrix, one removes the θ dependence in Hamiltonian (1), transformed in the intrinsic frame, and obtains

$$\begin{aligned} \hat{H}' &= \hat{U}(\theta)\hat{H}\hat{U}^{-1}(\theta) = \hat{H}_{\text{kin}} + \hat{H}_{\text{SOC}}, \\ \hat{H}_{\text{kin}} &= -i\gamma\left(\hat{\tau}_y \otimes I\partial_y + \hat{\tau}_x \otimes I\frac{1}{R}\partial_\theta\right), \\ \hat{H}_{\text{SOC}} &= -\lambda_y\hat{\tau}_y \otimes \hat{\sigma}_x - \lambda_x\hat{\tau}_x \otimes \hat{\sigma}_y. \end{aligned} \tag{6}$$

Here, the operators $\hat{\tau}_{x,y,z}$ are the Pauli matrices that act on the wave functions of the A and B sublattices (a pseudospin space), and

$$\lambda_x = \gamma(1 + 4\delta p)/(2R), \quad \lambda_y = \delta\gamma'/(4R) \tag{7}$$

are the strengths of the SOC terms. In the Hamiltonian (6) the term $\sim\lambda_x$ conserves, while the other one ($\sim\lambda_y$) breaks the spin symmetry in the armchair CNT.

The operator $\hat{J}_y$, being an integral of motion $[\hat{H}, \hat{J}_y] = 0$, is defined in the laboratory frame as

$$\hat{J}_y = I \otimes \left(\hat{L}_y + \frac{\hat{\sigma}_y}{2}\right) = I \otimes \left(-i\partial_\theta + \frac{\hat{\sigma}_y}{2}\right), \tag{8}$$

while in the intrinsic frame it is

$$\hat{J}_y \to \hat{J}'_y = \hat{U}\hat{J}_y\hat{U}^{-1} = I \otimes (-i\partial_\theta). \tag{9}$$

This integral allows us to present the wave functions as

$$F'(\theta, y) = e^{im\theta}e^{ik_y y}\Psi = e^{im\theta}e^{ik_y y}\begin{pmatrix} A \\ B \\ C \\ D \end{pmatrix}. \tag{10}$$

These wave functions are also the eigenfunctions of the other integral of motion, the operator $\hat{k}'_y \equiv \hat{k}_y$. Here, $m = \pm 1/2, \pm 3/2, \ldots$ is an eigenvalue of the angular momentum operator $\hat{J}'_y$. For the components of the eigenvector $F'(\theta, y)$ the relations $|A| = |D|$ and $|B| = |C|$ are fulfilled at real values of m and k_y.

Solving the eigenvalue problem $\hat{H}'F' = EF'$, one obtains the eigenspectrum

$$\begin{aligned} E &= \pm E_{m,q}, \quad E_{m,q} = \sqrt{t_m^2 + t_y^2 + \lambda_y^2 + \lambda_x^2 + 2D_{m,q}}, \\ D_{m,q} &= q\sqrt{\lambda_x^2(t_m^2 + \lambda_y^2) + t_y^2\lambda_y^2}, \quad q = \pm 1, \end{aligned} \tag{11}$$

where $t_m = \gamma m/R$, $t_y = \gamma k_y$.

B. Scattering model for one ripple

Keeping in mind what will be discussed below, we analyze the following geometry (see the construction profile in Fig. 1). It consists of one arc of a circle that is connected from the left-hand side to a flat graphene sheet. This (direct) arc is continuously connected to the inverse arc of the same radius that is connected to the right-hand flat graphene sheet. We put the origin of the coordinate at the center of the direct arc of the circle.

To give better insight into the scattering phenomenon in our model of a ripple, we study first only the direct arc of the circle connected to two flat surfaces. Two flat surfaces are (i) the region L, defined in the interval $-\infty < x < -R\cos\theta_0$, and (ii) the region R, defined in the interval $R\cos\theta_0 < x < \infty$. Region I is part of a nanotube of radius R, defined as $-R\cos\theta_0 < x < R\cos\theta_0$. At $\theta_0 = 0$, the ripple is half of the nanotube, while at $\theta_0 = \pi/2$ the ripple does not exist. For the sake of analysis we introduce the angle $\phi = \pi - 2\theta_0$.

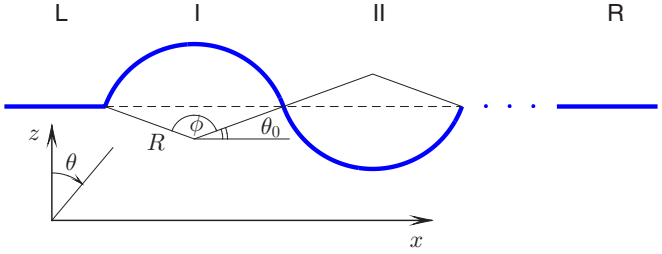

FIG. 1. (Color online) The rippled graphene system.

To describe the scattering phenomenon one has to define wave functions in different regions: flat (L, R) and curved (I) graphene surfaces.

Regions L and R are described by the Hamiltonian

$$\hat{H}_0 = \gamma(\hat{\tau}_x k_x + \hat{\tau}_y k_y) \otimes I, \tag{12}$$

which does not mix spin components. For the sake of simplicity, we consider the electron motion at normal incidence, with the electron wave vector $\vec{k} = (k_x,0)$. One solves the stationary Schrödinger equation $\hat{H}_0\Psi = E_0\Psi$ and obtains the corresponding eigenstates,

$$E_0 = \pm\gamma|k_x|, \tag{13}$$

$$\Psi = \exp(ik_x x)\Psi_0^\sigma(k_x), \tag{14}$$

$$\Psi_0^\sigma(k_x) = \frac{1}{2}\begin{pmatrix} \mathrm{sgn}(\gamma k_x E_0)\Phi_0^\sigma \\ \Phi_0^\sigma \end{pmatrix}, \tag{15}$$

$$\hat{\sigma}_y\Phi_0^\sigma = \sigma\Phi_0^\sigma, \quad \Phi_0^\sigma = \begin{pmatrix} 1 \\ i\sigma \end{pmatrix}, \quad \sigma = \pm 1. \tag{16}$$

Evidently, the wave functions in regions L and R can be written as a superposition of all possible solutions for flat graphene. To proceed, with the aid of eigenspinors (15) and (16), we introduce an auxiliary matrix $\hat{M}_0$ (4×4) for a given value of energy at the normal incidence

$$\hat{M}_0 = \left(\Psi_0^{+1}(K_x), \Psi_0^{-1}(K_x), \Psi_0^{+1}(-K_x), \Psi_0^{-1}(-K_x)\right). \tag{17}$$

Here, we define the variable $K_x = \mathrm{sgn}(\gamma E_0)|k_x|$ to ensure that the first two columns of the matrix M_0 correspond to eigenstates that move in a positive x direction, while the last two columns correspond to eigenstates that move in a negative x direction.

The matrix $\hat{M}_0$ is unitary, i.e., $\hat{M}_0^{-1} = \hat{M}_0^\dagger$. It allows us to define a general form of the wave function $\Psi_{L,R}$ for flat graphene,

$$\Psi_{L,R}(x) = \hat{M}_0 \exp[i\hat{K}(x - x_{L,R})]C_{L,R}, \tag{18}$$

where $\hat{K} = \mathrm{diag}(K_x, K_x, -K_x, -K_x)$ is a diagonal matrix, $x_{L,R}$ are x coordinates where flat and curved surfaces are connected, and $C_{L,R}$ are corresponding vectors with four unknown, yet normalized, coefficients in each region. Note that we do not consider inelastic scattering. Therefore, since the electron energy is conserved, we use the same vector $\vec{k} = (k_x,0)$ for the left and right flat graphene surfaces.

For the curved surface we use eigenspinors of the Hamiltonian (6). The general form of these eigenspinors is defined in the intrinsic frame [17]. Therefore, we apply the inverse transformation (5) to these eigenspinors in order to analyze the scattering problem in the laboratory frame. At $k_y = 0$ the spectrum (11) and the eigenspinors are particularly simple,

$$E_A = \pm\sqrt{t_m^2 + \lambda_y^2} + s\lambda_x, \quad s = \pm 1, \tag{19}$$

$$\Psi = \exp(im\theta)\ \Psi_A^s(t_m), \tag{20}$$

$$\Psi_A^s(t_m) = \begin{pmatrix} -s\Phi_A^s(t_m) \\ \sigma_y\Phi_A^s(t_m) \end{pmatrix}, \tag{21}$$

$$\Phi_A^s(t_m) = \exp\left(-i\frac{\theta}{2}\hat{\sigma}_y\right)\begin{pmatrix} -it_m \\ \lambda_y - (sE_A - \lambda_x) \end{pmatrix}. \tag{22}$$

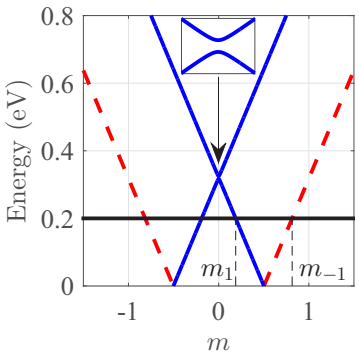

FIG. 2. (Color online) The spectrum (19) at $k_y = 0$ as a function of the quantum number m. Dashed red and solid blue lines are associated with states characterized by the quantum number $m_{s=-1}$ and $m_{s=+1}$, respectively. The values of $\pm m_s$ at the energy $E_F = 0.2$ eV (solid horizontal line) are indicated by vertical dashed lines. The parameters of calculations are $R = 10$ Å, $\delta = 0.01$, $p = 0.1$, $\gamma = \frac{9}{2}1.42$ Å eV, $\gamma' = \gamma\frac{8}{3}$, $\lambda_x = \frac{\gamma}{R}(1/2 + 2\delta p) = 0.32$ eV, $\lambda_y = \frac{\delta\gamma'}{4R} = 0.0043$ eV. The arrow indicates the gap displayed on the inset.

Note that energies in flat graphene and in a curved surface are different $E_0 = E_A + A(\frac{a}{R})^2$ (see details in Ref. [18]). This effect is caused by different hybridizations of π electrons in flat graphene and a graphene-based system with curvature. In particular, $A = 5/6, 7/12$ eV in the armchair and zigzag nanotubes, respectively.

At a fixed energy of the electron flow $E_0 \Leftrightarrow E_A$, Eq. (19) yields four possible values of the quantum number m:

$$m \Rightarrow m_s = \pm\frac{R}{\gamma}\sqrt{(sE_A - \lambda_x)^2 - \lambda_y^2}, \quad s = \pm 1. \tag{23}$$

Since the angular momentum is no longer the integral of motion, we have to consider the mixture of eigenfunctions with all possible values of m at a given energy.

As an example of the spectrum (19), a few positive energy branches as a function of the quantum number m are shown in Fig. 2. The branches are distinguished by the index $s = \pm 1$. There is an anticrossing effect between energy states characterized by the same $m_{s=+1}$ quantum number. This anticrossing is brought about by the interaction $\sim\lambda_y$ that breaks the spin symmetry (see Sec. II A) in the curved graphene surface. It results in a gap of $2\lambda_y$ near $E_A = \lambda_x$, indicated by the arrow (see the inset in Fig. 2). A similar gap occurs near $E_A = -\lambda_x$ for the m states with index $s = -1$. As a consequence of these gaps, evanescent modes arise at energies $\lambda_x - \lambda_y < |E| < \lambda_x + \lambda_y$ in our system. For the sake of illustration the positive spectrum (19) of m states is crossed by the horizontal line that mimics the Fermi energy. The crossing points determine quantum numbers m that have nonquantized values when the curved surface (arc of a circle) is connected to the flat one.

With the aid of eigenspinors (21) and (22) and the unitary transformation (5), we introduce an auxiliary matrix for a given value of energy at a curved surface,

$$\hat{M}_A(\theta) = \left(\Psi_A^1(t_{m_1}), \Psi_A^{-1}(t_{m_{-1}}), \Psi_A^1(-t_{m_1}), \Psi_A^{-1}(-t_{m_{-1}})\right)$$
$$= U(-\theta)\hat{M}_A(0). \tag{24}$$

As a result, in region I the wave function can be written as a superposition of all solutions for a curved surface in the form $\Psi_I(\theta) = \hat{M}_A(\theta)\exp(i\hat{m}\theta)C_I$. Here, C_I is a vector of four unknown coefficients, and $\hat{m} = \mathrm{diag}(m_1, m_{-1}, -m_1, -m_{-1})$ is a diagonal matrix.

The overlap of eigenspinors of the flat and bent regions can be readily calculated with the aid of Eqs. (15) and (21), which results in

$$\left(\Psi_0^\sigma\right)^\dagger\left(\Psi_A^s\right) \simeq [-\mathrm{sgn}(\gamma k_x E_0)s + \sigma] \times\left(\Phi_0^\sigma\right)^\dagger \exp\left(-i\frac{\theta}{2}\hat{\sigma}_y\right)\left(\Phi_A^s\right). \quad (25)$$

Evidently, the overlap is zero at $\sigma = \mathrm{sgn}(\gamma k_x E_0)s$. Note that already this result implies that some of the four channels between the flat and curved regions could be closed.

Matching the wave functions at the boundaries of regions L, I, and R, for an incoming electron flow from the left-hand side, leads us to the following equations:

$$\Psi_L(x_L) = \Psi_I(-\phi/2) \Rightarrow \hat{M}_0\begin{pmatrix}\Phi_{\mathrm{in}}\\ r\end{pmatrix} = \hat{M}_A(-\phi/2)C_I, \quad (26)$$

$$\Psi_R(x_R) = \Psi_I(+\phi/2) \Rightarrow \hat{M}_0\begin{pmatrix}t\\ 0\end{pmatrix} = \hat{M}_A(+\phi/2)\exp(i\hat{m}\phi)C_I. \quad (27)$$

We recall that the angles θ_0 and ϕ determine the $x_{L,R}$ coordinates: $x_L = R\cos(\theta_0+\phi)$, $x_R = R\cos\theta_0$. Here, $t = \binom{t(L)^{\mathrm{in}}_\uparrow}{t(L)^{\mathrm{in}}_\downarrow}$ and $r = \binom{r(L)^{\mathrm{in}}_\uparrow}{r(L)^{\mathrm{in}}_\downarrow}$ are transmission and reflection coefficients, respectively, for incoming an electron either with a spin up $|\uparrow\rangle \equiv \binom{1}{i}$ or with a spin down $|\downarrow\rangle \equiv \binom{1}{-i}$.

Solutions of Eqs. (26) (and similar equations for an incoming electron flow from the right-hand side) yield the following probabilities:

$$|t(L)^\uparrow_\uparrow|^2 = |t(R)^\downarrow_\downarrow|^2 = \frac{1}{1+(z_{-1})^2}, \quad (28)$$

$$|t(L)^\downarrow_\downarrow|^2 = |t(R)^\uparrow_\uparrow|^2 = \frac{1}{1+(z_{+1})^2}, \quad (29)$$

$$|r(L)^\uparrow_\downarrow|^2 = |r(R)^\downarrow_\uparrow|^2 = 1 - \frac{1}{1+(z_{-1})^2}, \quad (30)$$

$$|r(L)^\downarrow_\uparrow|^2 = |r(R)^\uparrow_\downarrow|^2 = 1 - \frac{1}{1+(z_{+1})^2}. \quad (31)$$

Here, we have also introduced the variable z_s,

$$z_s = \frac{\lambda_y \sin(m_s\phi)}{t_{m_s}} = \frac{\lambda_y R}{\gamma}\frac{\sin(m_s\phi)}{m_s}, \quad s = \pm 1, \quad (32)$$

related to the characteristics of the curved surface (see Sec. II A).

Evidently, there is no backscattering for incoming electrons if $\lambda_y = 0$ [see Eqs. (30)–(32)]. However, at $\lambda_y \neq 0$ backscattering with a spin inversion takes place. The reflection probabilities without the spin inversion are $|r(L)^\uparrow_\uparrow|^2 = |r(L)^\downarrow_\downarrow|^2 = 0$. The same is true for the transmission probabilities with a spin inversion, i.e., $|t(L)^\uparrow_\downarrow|^2 = |t(L)^\downarrow_\uparrow|^2 = 0$. Thus, backscattering with a spin inversion is nonzero in the ripple due to the curvature-induced SOC produced by the λ_y term. In addition, incoming electrons with different spin orientations choose different channels (different $m_s, s = \pm 1$).

The maximum transmission probability $|t(L)^\uparrow_\uparrow|^2 = 1$ takes place at the condition

$$m_{-1}\phi_c = \pi n, \quad n = 1,2,\ldots \quad (33)$$

[see Eqs. (28) and (32)]. Evidently, this probability becomes dominant at the minimum transmission $|t(L)^\downarrow_\downarrow|^2$. The lowest minimum of the transmission $|t(L)^\downarrow_\downarrow|^2$ occurs at the condition $E_A = \lambda_x$, when m_{+1} becomes imaginary [see Eq. (23)]. In other words, the propagating mode transforms to the evanescent mode for the channel m_{+1}. Taking into account the condition $E_A = \lambda_x$ in Eq. (23), one obtains the critical angle of the curved surface (in the form of the arc) for a maximum of spin-up filter efficiency,

$$\phi_c = \frac{\pi n}{m_{-1}} = \frac{\pi n\gamma}{R\sqrt{4\lambda_x^2 - \lambda_y^2}}, \quad (34)$$

where the SOC strengths $\lambda_{x,y}$ are defined by Eq. (7). For parameters listed in the caption of Fig. 2 we have $|\phi_c| \approx 0.996\pi$ ($n = 1$). For the same critical angle ϕ_c and $E_A = -\lambda_x$ we obtain a maximum for the spin-down filter efficiency, when m_{-1} becomes imaginary.

Thus, there are different channels for the spin-up and spin-down electron (hole) flows. Note that the deviation from the energy value $E_A = \pm\lambda_x$ could produce the equal transmission for spin-up and spin-down electrons [see Fig. 3(a)]. Therefore, it is important to choose the energy $|E_A|$ to be in the close vicinity of the energy value $\simeq\lambda_x$. For the considered parameters the filter efficiency is, however, small. So far this result has met with only limited success.

C. Scattering model for *N* ripples

To increase the efficiency we suggest connecting the bent parts sequentially, as shown in Fig. 1. In particular, the construction with the direct plus inverse arcs (with the same angle ϕ) transforms Eqs. (26) and (27) to the forms

$$\hat{M}_0\begin{pmatrix}\Phi_{\mathrm{in}}\\ r\end{pmatrix} = \hat{M}_A(-\phi/2)C_I, \quad (35)$$

$$\hat{M}_0\begin{pmatrix}t\\ 0\end{pmatrix} = \hat{M}_A(\pi-\phi/2)\exp(-i\hat{m}\phi) \times\hat{M}_A^{-1}(\phi/2-\pi)\hat{M}_A(+\phi/2)\exp(+i\hat{m}\phi)C_I. \quad (36)$$

Since in the inverse arc the phases, accumulated from the point of connection with the direct arc to the point of connection with a straight line (flat graphene), have a sign opposite that of the first one, we use $\exp(\pm i\hat{m}\phi)$.

Matching the wave functions at the boundaries of regions L, I, II, and R for electrons coming from the left-hand (L) and right-hand (R) sides of the construction leads us to the

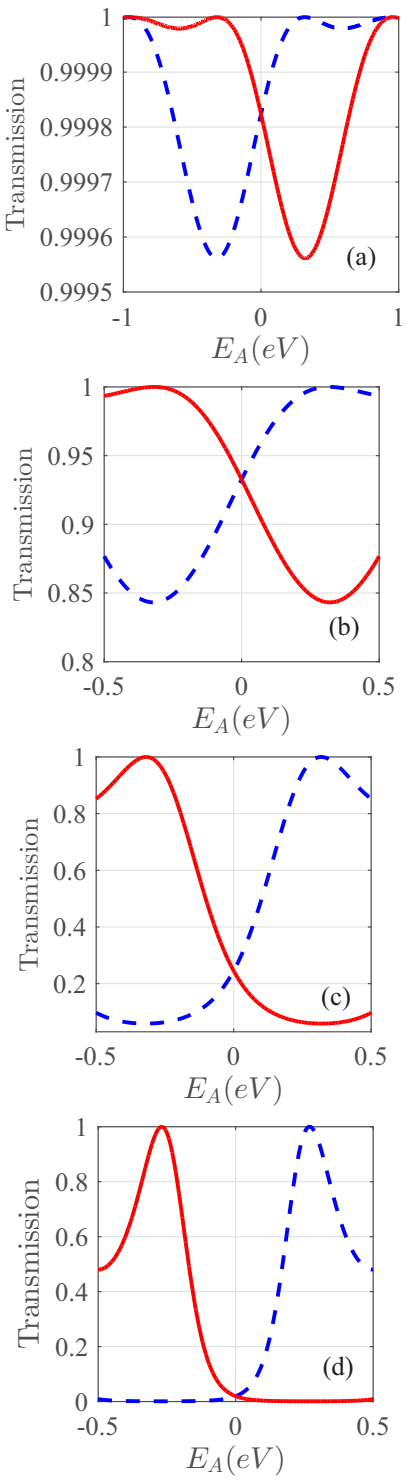

FIG. 3. (Color online) Dependence of transmission probabilities $|t(L)^{\uparrow}_{\uparrow}|^2$ (blue dashed lines) and $|t(L)^{\downarrow}_{\downarrow}|^2$ (red solid lines) on the energy E_A at $k_y = 0$ for (a) 1, (b) 20, (c) 100, and (d) 200 sequentially connected ripples (π arcs). The parameters are the same as in Fig. 2.

following nonzero probabilities:

$$|t(L)^{\uparrow}_{\uparrow}|^2 = \left[\frac{1}{1+2(z_{-1})^2}\right]^2 = |t(R)^{\downarrow}_{\downarrow}|^2, \tag{37}$$

$$|t(L)^{\downarrow}_{\downarrow}|^2 = \left[\frac{1}{1+2(z_{+1})^2}\right]^2 = |t(R)^{\uparrow}_{\uparrow}|^2, \tag{38}$$

$$|r(L)^{\uparrow}_{\downarrow}|^2 = 1 - |t(L)^{\uparrow}_{\uparrow}|^2 = |r(R)^{\downarrow}_{\uparrow}|^2, \tag{39}$$

$$|r(L)^{\downarrow}_{\uparrow}|^2 = 1 - |t(L)^{\downarrow}_{\downarrow}|^2 = |r(R)^{\uparrow}_{\downarrow}|^2. \tag{40}$$

Thus, the transmissions through one and two (direct plus inverse) arcs are accompanied by the inverse backscattering. The considered cases imply that the larger the number of arcs is, the stronger the inverse backscattering is for one of the spin components.

Following the recipe described in Ref. [19] (interfering Feynman paths) and combining S matrices for N connected arcs, we obtain

$$|t(L)^{\uparrow}_{\uparrow}|^2 = \left[\frac{2}{C^{(+)^N}_{-1} + C^{(-)^N}_{-1}}\right]^2 = |t(R)^{\downarrow}_{\downarrow}|^2, \tag{41}$$

$$|t(L)^{\downarrow}_{\downarrow}|^2 = \left[\frac{2}{C^{(+)^N}_{+1} + C^{(-)^N}_{+1}}\right]^2 = |t(R)^{\uparrow}_{\uparrow}|^2. \tag{42}$$

Here, the variable $C^{(\pm)}_s$ is defined as

$$C^{(\pm)}_s = \sqrt{1+(z_s)^2} \pm z_s, \quad s = \pm 1. \tag{43}$$

Evidently, at $z_s = 0$ the transmission probability is 1 for any number of arcs, while $z_s \neq 0$ leads to the decrease of the transmission probability with the increase of the number of arcs. The suppression is, however, different for various transmission probabilities due to their different dependence on the quantum number m_s.

As shown above, conditions (33) and (34) determine the dominance, in particular, of the transmission probability of spin-up incoming electrons at $E_A > 0$. Indeed, a set $N \gg 1$ of an exact replica of the consistently connected ripples (see Fig. 1) does not affect this dominance ($= 1$) for the $m_{s=-1}$ channel. However, this set suppresses the spin-down transmission probability for the $m_{s=+1}$ channel that is proportional to $x < 1 \Rightarrow x^N \to 0$.

We would like to point out that Eqs. (41) and (42) are valid for odd and even numbers of consistently connected ripples. In our model the only requirement is that the direct ripple has to be connected to the inverse one, the inverse ripple to the direct one, etc. From our consideration it follows that, if at a certain energy, for example, $E_A > 0$, there is a high transmission probability for *spin-up* electrons from the left side of our system, one obtains the same magnitude for the transmission probability for *spin-down* electrons from the right side.

III. DISCUSSION

A. *N* factor

To obtain a simple picture of the physics behind the enhancement of the spin-filtering effect, let us consider the transmission at the energy $E_A \simeq \lambda_x$, when m_{+1} becomes imaginary [see Eq. (23)] and the propagating mode transforms to the evanescent mode for the channel m_{+1}. In light of Eqs. (23) and (7), one obtains

$$m_{+1} = i\frac{R}{\gamma}\lambda_y = ix, \quad x = \frac{\delta\gamma'}{4\gamma} \approx 0.007. \tag{44}$$

As a result, the variable z_+ [Eq. (32)] transforms into the form

$$z_+ \simeq x\phi \ll 1. \tag{45}$$

Taking into account Eqs. (43)–(45), one can readily estimate that at $N \gg 1$,

$$C_{+1}^{(+)N} + C_{+1}^{(-)N} \simeq 2 + (Nx\phi)^2 \tag{46}$$

$$\Rightarrow |t(L)_{\downarrow}^{\downarrow}|^2 \approx \left[\frac{2}{2 + (Nx\phi)^2}\right]^2. \tag{47}$$

With our choice of parameters and $\phi \simeq \pi$, this result yields

$$|t(L)_{\downarrow}^{\downarrow}|^2 \ll 1 \Longleftrightarrow N \gg \frac{1}{x\pi} \approx 45. \tag{48}$$

The illustration of this phenomenon is displayed in Fig. 3 for the transmission probabilities through 1, 20, 100, and 200 sequentially connected ripples (π arcs). Here, we consider the transmission as a function of the curved surface energy E_A of the incoming electrons (holes). A small difference between spin-up and spin-down transmission probabilities for one ripple [Fig. 3(a)] at $E_A > 0$ evolves to $\simeq$100% efficiency for the spin-up transmission probabilities for the left-side incoming electron at $N = 200$ ripples [Fig. 3(d)]. The opposite picture takes place for the spin-down transmission probabilities at $E_A < 0$. To realize such a situation one might use the SiO_2 substrate as a gate of the curved surface, which helps control the concentration of charge carriers in graphene. As a result, one can change the charge carrier type from electron to hole [20].

B. Spin filtering and ripple parameters R and ϕ

In light of the above analysis, without loss of generality, we can consider $m_s\phi < 1$ in order to observe the suppression effect [see Eq. (48)]. With the aid of Eq. (23), taking into account that $\lambda_x \gg \lambda_y$, this requirement leads to the following inequality:

$$\lambda_x - \frac{\gamma}{R\phi} < |E_A| < \lambda_x + \frac{\gamma}{R\phi}. \tag{49}$$

To remain at the maximum, for example, the transmission probability $|t(L)_{\uparrow}^{\uparrow}|^2 = 1$, it is necessary to fulfill condition (33). As a result, in light of Eq. (23) and the condition $\lambda_x \gg \lambda_y$, taking into account Eq. (7), we obtain

$$R \simeq \frac{\gamma}{|E_A|}\left(\frac{\pi}{\phi} - \beta\right), \quad \beta = \frac{1 + 4\delta p}{2}. \tag{50}$$

Combining this equation with Eq. (49), we have

$$\frac{\pi - 1}{2\beta} < \phi < \frac{\pi + 1}{2\beta}. \tag{51}$$

Thus, Eqs. (50) and (51) determine the region of feasibility of the parameters R and ϕ, where the spin-filtering effects could exist at fixed system (graphene) parameters such as γ, δ, and the electron energy E_A. From this observation, two arguments follow in favor of our findings. First, even at $\phi \neq \phi_c$ [see Eq. (34)] one of the spin components in the incoming electron (hole) flow is suppressed for a large enough number of ripples at some particular energy region. Second, we assume that all ripples are identical. Practically, the graphene surface is randomly curved, and it is a real challenge to create identical, consequently connected ripples. However, it is our belief that modern technology will allow us to realize this situation sooner or later. Whatever the case, the spin-filtering effect should survive if small variations of radii and angles of consequently connected ripples are subject to conditions (50) and (51) at a fixed value E_A of the electron energy flow.

C. Effect of a finite k_y momentum

In our model a single ripple is modeled as part of a nanotube that is infinite in the y direction. Evidently, realistic ripples are limited in space in both the x and y directions. In particular, graphene nanoribbons are considered prominent candidates to control the electronic properties of graphene-based devices. This issue requires, however, a dedicated study and is the subject of a forthcoming paper.

In order to have some idea of what should be expected in graphene nanoribbons, we analyze the case with a finite $k_y \neq 0$. Nonzero k_y could mimic the case of a ripple limited in the y direction. Indeed, a finite width in the y direction introduces the quantization of the k_y momentum on the curved surface. As a result, the eigenspinors at the curved surface would depend on the mixture $\pm k_y$ values for $s = \pm 1$, i.e., altogether four-momentum k_y (see details in Ref. [17]). In this case analytical expressions are too cumbersome, even in a simple case of one conserved momentum k_y on the curved surface. Therefore, we proceed with a numerical analysis that provides a vivid presentation of a simple case with a single value of the k_y momentum on the curved surface.

Let us suppose that the incoming electron flow possesses a momentum $\vec{k} = (k_x, k_y)$ in regions L and R. Evidently, in this case $E_0 = \pm\gamma\sqrt{k_x^2 + k_y^2}$. For simplicity, we consider $E_0 > 0$ and obtain for the momentum on the curved surface

$$k_y = t_y/\gamma = (E_0/\gamma)\sin(\alpha). \tag{52}$$

The results of the calculations exhibit a degradation of the spin-filter ability of our system. At a fixed value of the energy $E_0 = \lambda_x$ the transmission probability $|t(L)_{\uparrow}^{\uparrow}|^2$ decreases drastically at $|\alpha| \geqslant \pi/8$ [see Fig. 4(a)]. It seems that the spin-filtering effects would survive at $|\alpha| < \pi/8$. Note, however, that this estimation depends on the system parameters, such as γ and E_0.

At a fixed value of the momentum k_y the effectivity of spin filtering is reduced by $\sim$10% [see Fig. 4(b)]. At the same time, our systems manifests a zero transmission for all spin orientations for charge carriers at energies -0.06 eV $< E_A <$ 0.06 eV due to our choice of the value k_y.

D. The graphene purity

We restricted our consideration to a ballistic regime. This approximation is well justified due to the following factors. The remarkable strength of the carbon honeycomb lattice makes it quite difficult to introduce any defects into the lattice itself. Charge impurities that could limit electron mobility in graphene are still an open problem from both experimental and theoretical points of view (see, for example, discussion in Ref. [1]). It is also well known that the difference in conductivity in graphene between $T \approx 0$ and room temperature is no

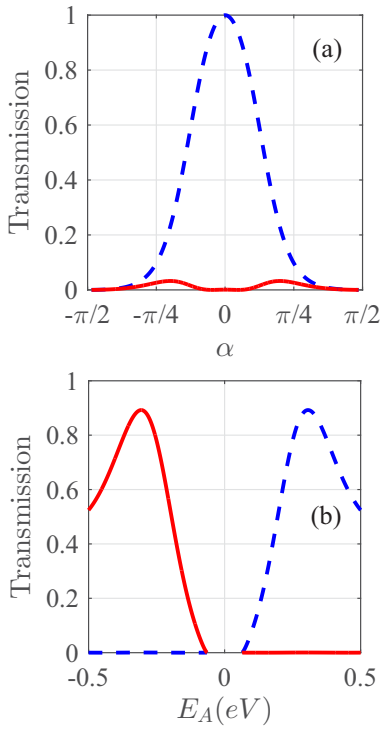

FIG. 4. (Color online) Transmission probabilities $|t(L)^{\uparrow}_{\uparrow}|^2$ (blue dashed lines) and $|t(L)^{\downarrow}_{\downarrow}|^2$ (red solid lines) (a) as a function of the incidence angle α at $E_0 = E_A = \lambda_x = 0.32$ eV and (b) as a function of the energy E_A at $k_y = 0.01$ Å^{-1}. The calculations are done for 200 sequentially connected ripples (π arcs). The other parameters are the same as in Fig. 2.

more than a few percent. In other words, the electron-phonon scattering plays a minor role.

We recall that a typical ripple size is ∼7 nm (see Ref. [21]). In our paper the ripple is modeled as the curved surface in the form of an arc of a circle with a radius $R = 1$ nm. As a result, our system length is $\pi R \times 200 \approx 640$ nm. Taking into account that a typical mean free path of electrons in single-wall nanotubes is $\ell \approx 1$ μm (see, e.g., Ref. [2]), it seems our consideration is on a reasonable basis.

Thus, in our model the basic mechanism that is responsible for spin-filtering effects is an attenuation of one of the transmitting modes. It transforms to the evanescent mode in the energy gap created by the SOC in the curved surface. The multiplicative action of a large enough number of ripples suppresses this transmitting mode at certain conditions that provide a high efficiency for the other one.

IV. SUMMARY

We have analyzed the transmission and reflection of ballistic electron flow through a ripple in an effective-mass approximation when only the interaction between nearest-neighbor atoms is taken into account. In our consideration a ripple consists of the curved surface in the form of an arc of a circle connected from the left-hand and right-hand sides to two semi-infinite flat graphene sheets. Considering the curved surface as part of the armchair nanotube, we have shown that the curvature-induced spin-orbit coupling yields backscattering [see Eqs. (30) and (31)] with spin inversion. This spin inversion is caused by the spin-orbit term that breaks spin symmetry (a spin projection on the symmetry axis) in the effective Hamiltonian of the armchair CNT.

In the energy gap created by the curvature-induced spin-orbit coupling there is a preference for one spin orientation, depending on the direction of the electron flow at normal incidence. The width of the energy gap depends in inverse proportion on the radius of the ripple. At this energy range the ripple acts as a semipermeable membrane which is more transparent for the incoming electrons with spin up from the left-hand side and with spin down from the right-hand side and *vice versa* for the holes. In other words, there is a precursor of *chiral* transmission of spin components of the incoming electron (hole) flow at a fixed energy. For one ripple system this effect is, however, small. In order to enforce this effect, we extended our consideration to a curved surface of the sinusoidal wave type with N arcs. This step is of crucial importance to suppress one of the spin components and to support the spin inversion symmetry for the transmission probability. The larger the number of consistently connected ripples (arcs) is, the stronger the dominance of a specific spin component is in comparison with the other in the transmission from the same direction. There is a cooperative effect of *chiral spin* transmissions produced by a large number of ripples. To trace the N dependence we have derived a formula for a composite transmission probability for well-polarized spin components: (i) Eq. (41) for spin-up electrons and (ii) Eq. (42) for spin-down electrons. Based on these results, we predict a strong spin-filtering effect for a sufficiently large number of arcs in the rippled graphene system. In contrast to the usual waveguide that guides optical or sound waves of a chosen frequency in a well-defined direction, our system guides spin electron (hole) waves with a well-defined polarization in one or another direction at a certain energy. It seems, therefore, natural to name this system *chiral spin guide*.

We have considered only a curved surface that owes its origin to an armchair nanotube. Evidently, our model can be extended to other types of origins. However, the corresponding analysis requires a separate study. We also neglected the effective magnetic field that arises from the dependence of the hopping parameter γ on the curvature (see discussion in [3]). This effect influences the local density of states [22]. It can cause the localization of the electrons on the boundary between flat graphene and the curved surface, similar to the boundary state for some types of carbon nanoparticles [23]. As a result, it might affect the efficiency of the spin guide. Last, but not least, many-body effects such as electron-electron interaction should be incorporated and analyzed as well. It is especially noteworthy that electron-electron interaction, designed in the form of a specific potential barrier on the graphene sheet [24], leads to separation of spin-polarized states. In fact, this result is in close agreement with our finding, obtained for one ripple. As mentioned above, the curvature-induced SOC simulates a penetrable barrier preferable for transmission of only one of two spin components, depending on the direction and energy of the incoming electron (hole) flow. It would be interesting to study the interplay between the SOC and electron-electron interaction on the electron transport in our system. Evidently,

this consideration would allow us to study in more detail the effect of impurities on the electron mobility in our system.

In conclusion, the transparency and the mathematical rigor of our results provide good grounds to believe that spin-filtering effects found in this paper, giving rise to a chiral spin-guide phenomenon, will be observable in experiment.

ACKNOWLEDGMENTS

M.P. and K.N.P. are grateful for the warm hospitality and creative atmosphere at UIB and JINR. This work was supported in part by Russian Foundation for Basic Research Grant No. 14-02-00723 and Vedecká Grantová Agentúra MŠVVaŠ SR a SAV (2/0037/13).

[1] M. I. Katsnelson, *Graphene: Carbon in Two Dimensions* (Cambridge University Press, Cambridge, 2012).
[2] L. E. F. Foa Torres, S. Roche, and J.-C. Charlier, *Introduction to Graphene-Based Nanomaterials* (Cambridge University Press, New York, 2014).
[3] M. Katsnelson and A. Geim, Philos. Trans. R. Soc. A **366**, 195 (2008)
[4] W. Bao, F. Miao, Z. Chen, H. Zhang, W. Jang, C. Dames, and C. Lau, Nat. Nanotechnol. **4**, 562 (2009).
[5] H. Min, J. E. Hill, N. A. Sinitsyn, B. R. Sahu, L. Kleinman, and A. H. MacDonald, Phys. Rev. B **74**, 165310 (2006).
[6] T. Ando, J. Phys. Soc. Jpn. **69**, 1757 (2000).
[7] M. V. Entin and L. I. Magarill, Phys. Rev. B **64**, 085330 (2001).
[8] A. De Martino, R. Egger, K. Hallberg, and C. A. Balseiro, Phys. Rev. Lett. **88**, 206402 (2002).
[9] D. Huertas-Hernando, F. Guinea, and A. Brataas, Phys. Rev. B **74**, 155426 (2006).
[10] F. Kuemmeth, S. Ilani, D. C. Ralph, and P. L. McEuen, Nature (London) **452**, 448 (2008).
[11] D. V. Bulaev, B. Trauzettel, and D. Loss, Phys. Rev. B **77**, 235301 (2008).
[12] L. Chico, M. P. López-Sancho, and M. C. Muñoz, Phys. Rev. B **79**, 235423 (2009).
[13] J.-S. Jeong and H.-W. Lee, Phys. Rev. B **80**, 075409 (2009).
[14] W. Izumida, K. Sato, and R. Saito, J. Phys. Soc. Jpn. **78**, 074707 (2009).
[15] M. del Valle, M. Margańska, and M. Grifoni, Phys. Rev. B **84**, 165427 (2011).
[16] J. Klinovaja, M. J. Schmidt, B. Braunecker, and D. Loss, Phys. Rev. B **84**, 085452 (2011).
[17] K. N. Pichugin, M. Pudlak, and R. G. Nazmitdinov, Eur. Phys. J. B **87**, 124 (2014).
[18] M. Pudlak and R. Pincak, Eur. Phys. J. B **67**, 565 (2009).
[19] S. Datta, *Electronic Transport in Mesoscopic Systems* (Cambridge University Press, Cambridge, 2007).
[20] S. V. Morozov, K. S. Novoselov, and A. K. Geim, Phys. Usp. **51**, 744 (2008).
[21] A. Fasolino, J. H. Los, and M. I. Katsnelson, Nat. Mater. **6**, 858 (2007).
[22] F. de Juan, A. Cortijo, and M. A. H. Vozmediano, Phys. Rev. B **76**, 165409 (2007).
[23] T. Fujita, M. B. A. Jalil, S. G. Tan, and S. Murakami, J. Appl. Phys. **110**, 121301 (2011).
[24] L. Ying, G. Wang, L. Huang, and Y. C. Lai, Phys. Rev. B **90**, 224301 (2014).